electronics

Article

An H-Plane Groove Gap Waveguide Magic-T for X-Band Applications

Riccardo Rossi and Roberto Vincenti Gatti *

Department of Engineering, University of Perugia, Via G. Duranti 93, 06125 Perugia, Italy
* Correspondence: roberto.vincentigatti@unipg.it

Abstract: An X-band H-plane groove gap waveguide magic-T is presented as a combination of an H-plane and an E-plane T-junction. Two architectures can be derived by orientating the sum and difference ports to the same or opposite directions, respectively. Slot coupling allows the reduction of the device dimensions along the E-plane, and such a low profile can be attractive in all groove gap waveguide applications where compactness is required. A proof-of-concept prototype is fabricated with standard low-cost CNC milling machine manufacturing techniques. Good agreement between simulations and measurements is observed.

Keywords: gap waveguide; magic-T; X-band

check for updates

Citation: Rossi, R.; Vincenti Gatti, R. An H-Plane Groove Gap Waveguide Magic-T for X-Band Applications. *Electronics* **2022**, *11*, 4075. https://doi.org/10.3390/electronics11244075

Academic Editor: Alejandro Melcón Alvarez

Received: 16 November 2022
Accepted: 5 December 2022
Published: 8 December 2022

1. Introduction

The magic-T is an essential component in a wide range of applications, such as radar and communication systems, microwave circuits and measurement setups. When the sum port is excited, no power flows to the difference port due to even symmetry, while there is an in-phase and equal-split power division at the co-linear ports. In contrast, when the difference port is excited, no power flows to the sum port due to odd symmetry, while power is equally divided at the co-linear ports, this time with a 180° phase shift. When two signals arrive at the co-linear ports, their sum and their difference are obtained at the sum port and at the difference port, respectively. Matching at all ports is obtained by means of proper tuning elements. These features make the device appealing for those applications where power dividing/combining with high output port isolation is required [1].

The magic-T has been presented in different technologies over the years, such as microstrip [2,3], substrate-integrated waveguide (SIW) [4–8] and low-temperature co-fired ceramics (LTCC) [9,10]. Despite being lightweight and low-cost, these devices are limited by dielectric losses and low power-handling capabilities. For these reasons, hollow waveguide implementations have been introduced and preferred in high-power and high-performance systems [11–24]. Nevertheless, the majority of waveguide magic-Ts presents output ports pointing in different directions, and this could represent a drawback in all cases where compactness is desired. In addition to this, hollow waveguide components are manufactured using split blocks and joined together by screwing, deep-brazing or diffusion bonding. Severe leakage can be caused by small gaps on the blocks' contact surfaces, thus a very reliable electrical contact between the fabricated parts as well as good alignment are mandatory. High-precision manufacturing and assembling are required as the operating frequency is increased, thus leading to a higher cost. The gap waveguide technology has recently been proposed to overcome these problems.

The ideal gap waveguide derives from separating two parallel plates, in particular a perfect magnetic conductor (PMC) and a perfect electric conductor (PEC), with an air gap smaller than a quarter wavelength [25,26]. In this way, no wave can propagate between the plates. Since a PMC cannot be found in nature, its condition is emulated by an artificial magnetic conductor (AMC) in the form of periodic textured structures, among which the

most known is the bed of nails realized by periodic metal pins. This high-impedance surface creates a stopband over which parallel-plate modes propagation is forbidden. The groove gap waveguide (GGW) and the ridge gap waveguide (RGW) originate from incorporating in the bed of nails two guiding structures in the form of a groove or a ridge, respectively. In this way, as a consequence of the stopband, the electromagnetic wave is confined in the groove or above the ridge without leaking in lateral directions. The GGW and RGW are very similar to the traditional rectangular waveguide and ridge waveguide, with the exception that a good electrical contact between the upper and lower metal surfaces is no longer necessary, thus relaxing mechanical requirements with a consequent cost reduction. Moreover, the absence of a dielectric makes this technology suitable for the design of low-loss components with high power-handling capabilities.

The literature on magic-Ts in gap waveguide technology is not vast. A Ka-band design is presented in Ref. [27] for millimeter-wave applications. The device adopts a GGW T-junction for the sum and the co-linear ports and a standard rectangular waveguide (RW) for the difference port. Matching is primarily achieved through a five-step conducting cone. The difference port is perpendicular to the bottom layer, as in traditional hollow waveguide designs, thus entailing a bulky volume. For this reason, slot coupling or same-layer architectures are preferred for size reduction. A W-band prototype is proposed in Refs. [28,29] for monopulse tracking radars. The component uses a RGW T-junction as a lower layer, coupled to a GGW upper layer through a slot. A tapered ridge and a small step serve as matching elements. The Ka-band magic-T in Ref. [30] for monopulse radar applications uses a RGW T-junction for the sum port and an E-plane GGW for the difference port on the same layer. Three metal windows and a metal step are inserted for impedance matching and act as capacitive and inductive loads, respectively. However, in all works referenced so far, a hybrid architecture is always described, i.e., the sum and difference ports are realized in two different technologies, be they RGW, GGW or RW. A full E-plane GGW magic-T is illustrated in Ref. [31] for Ka-band monopulse antenna systems. The four ports are arranged in the same layer and the difference port is coupled to the remaining ones through a thin metal ridge.

In this paper, an H-plane T-junction and an E-plane T-junction in H-plane GGW technology are presented and combined in the design of an H-plane GGW magic-T operating at X band. To the best of the authors' knowledge, this is the first time that this technology is employed for all the four ports of the device. Two configurations are proposed, namely T-shaped and cross-shaped (or X-shaped), depending on the sum and difference ports lying on the same side or on opposite sides, respectively. An X-shaped magic-T is manufactured and tested and experimental results validate the design procedure. All simulations are performed using the commercial 3D full-wave software CST Microwave Studio.

2. Groove Gap Waveguide Design

The gap waveguide stopband is defined as the frequency interval for which parallel-plate modes cannot propagate. This interval depends on the gap waveguide geometrical parameters such as the pin side q, the pin height d, the pitch between two adjacent pins p and the air gap height h. An appropriate GGW geometry for X-band operation is selected in agreement with Ref. [32] and illustrated in Figure 1.

From now on, the air inside a metal background is illustrated and top metal layers are hidden for better clarity. Pins are arranged according to a square lattice and the bed of nails is truncated on each side after the third row of pins, with no performance deterioration [33]. The material adopted in the following simulations is PEC with zero surface roughness. PEC boundary conditions surround the transversal walls.

With resemblance to a standard RW, a dispersive mode very similar to the TE_{10} mode propagates inside the groove within the stopband. The GGW dispersion diagrams are calculated using the eigenmode solver in CST Microwave Studio, and are presented in Figure 2. From an analysis of the first eight propagating modes, the resulting stopband covers the whole X band, ranging from 7.86 GHz to 13.07 GHz. It is well known that

full-wave software requires continuous cross-section waveguide ports. Similarly to the RW, numerical ports are usually attached to the GGW [34], although perfect impedance matching may not be guaranteed. For this reason, an equivalent RW can be defined, with width a and height $b = d + h$, and separated from the first row of pins by a distance k. The values for a and k for the geometry of Figure 1 are chosen for optimum return loss, as reported in Figure 3 for the whole stopband.

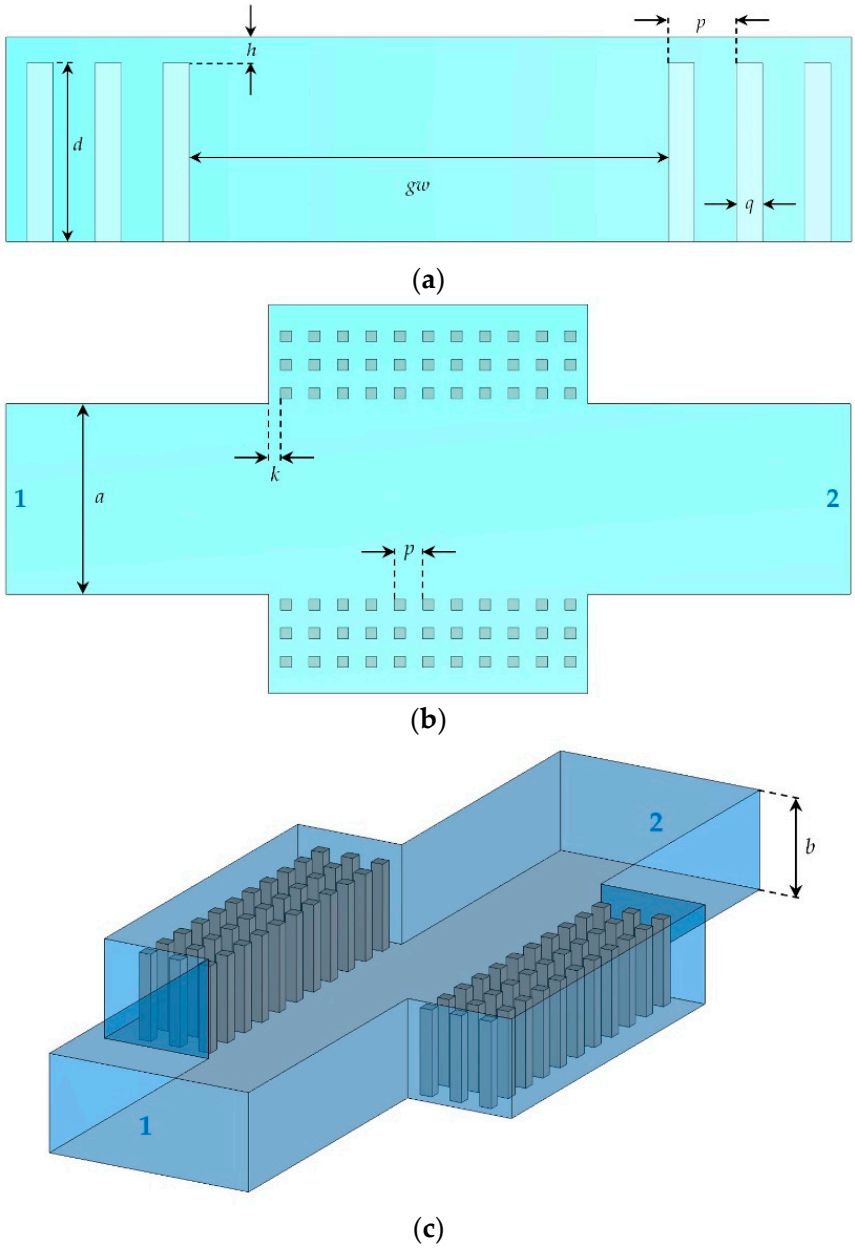

Figure 1. Groove gap waveguide geometry. (**a**) Cross section. (**b**) Top view. (**c**) 3D view.

The propagation constant of the equivalent RW is also plotted in Figure 2, indicating a strong similarity between the fundamental modes of the two waveguides in the designated bandwidth. Figure 4 clearly shows that the electric field is almost nonexistent after the third row of pins, as expected. The GGW geometrical parameters are listed in Table 1.

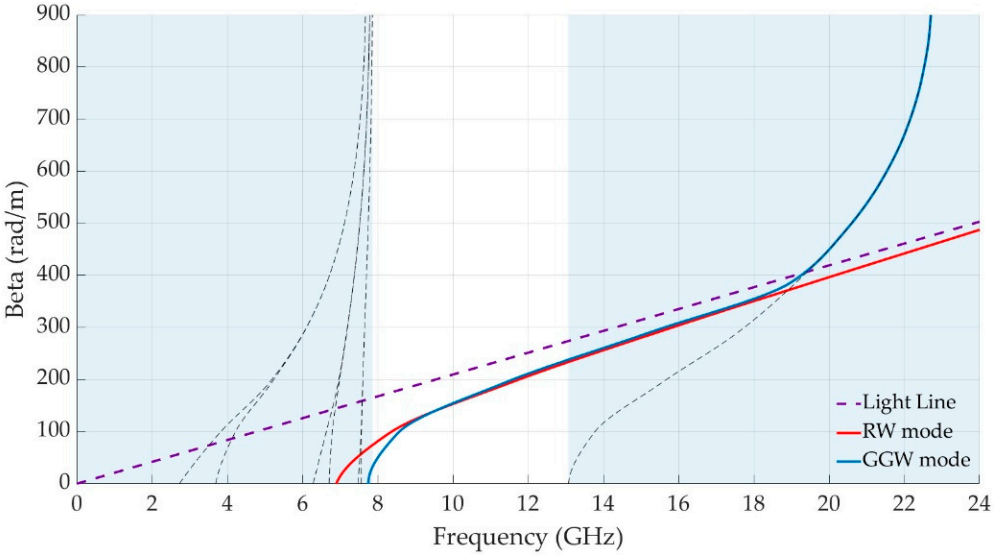

Figure 2. Groove gap waveguide dispersion diagrams. Solid blue curve is the only mode propagating in the stopband. Black Dashed curves are the modes propagating outside the stopband.

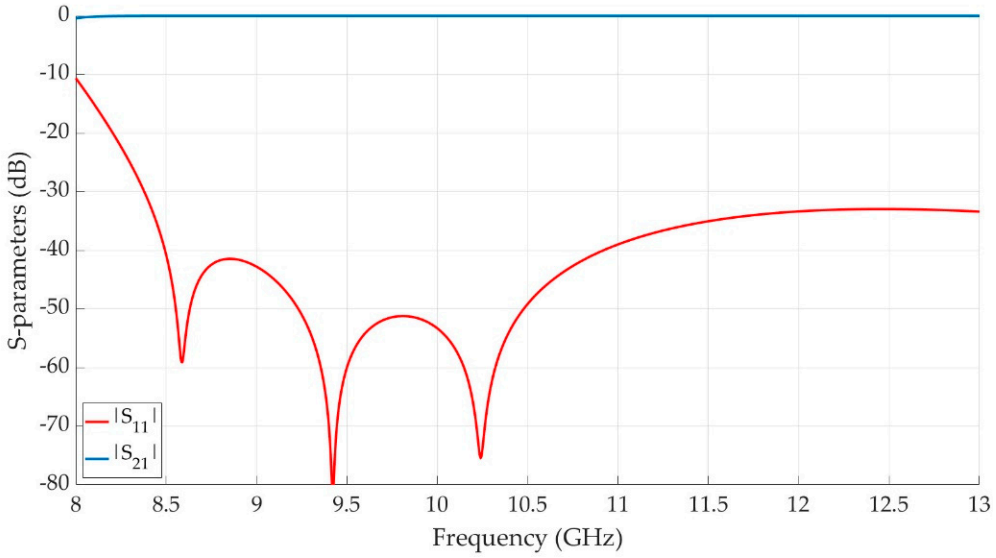

Figure 3. Groove gap waveguide scattering parameters.

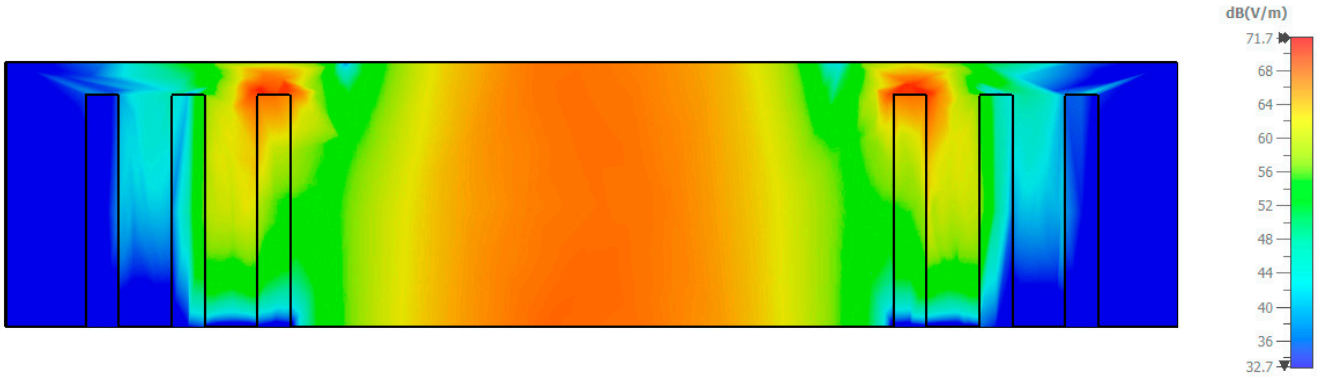

Figure 4. Groove gap waveguide cross-section electric field @ 9.5 GHz.

Table 1. Groove gap waveguide geometrical parameters.

Parameter	Description	Value (mm)
a	Eq. waveguide width	21.70
b	Eq. waveguide height	10.00
d	Pin height	8.75
gw	Groove width	22.86
h	Air gap separation	1.25
k	Eq. waveguide distance	1.37
p	Pin pitch	3.25
q	Pin side	1.25

3. T-Junctions Design

Since a magic-T is the combination of an H-plane T-junction and an E-plane T-junction with common co-linear ports, the design of both junctions is a preliminary step for the final component. In this paper, all devices operate at a center frequency of 9.5 GHz.

The H-plane T-junction geometry is shown in Figure 5. The architecture is similar to a classical RW junction, with inductive irises at the junction between the input and output ports with width and height equal to the GGW pins and a tuning post acting as a metal septum again with the same dimensions of the GGW pins. A small central square block introduces a localized capacitance which improves impedance matching. The H-plane T-junction geometrical parameters and simulated scattering parameters are reported in Table 2 and Figure 6, respectively. The return loss is better than 20 dB from 8.95 to 10.20 GHz, corresponding to a 13.05% fractional bandwidth. Equal power division is observed in the same frequency interval.

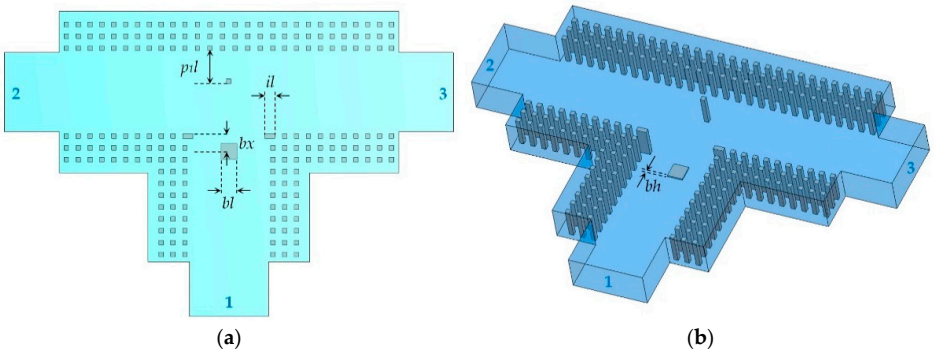

Figure 5. H-plane T-junction geometry. (**a**) Top view. (**b**) 3D view.

Table 2. H-plane T-junction geometrical parameters.

Parameter	Description	Value (mm)
bh	Block height	0.50
bl	Block length	4.38
bx	Block offset	4.92
il	Iris length	2.86
p_1l	Post 1 length	9.01

The E-plane T-junction geometry is shown in Figure 7. Port 1 lies in the upper layer, with ports 2 and 3 in the lower layer. These layers are coupled by means of a symmetrical slot excited by a post with the same dimensions of the GGW pins. The GGW short distance with respect to the slot center is optimized for impedance matching. Internal edges are rounded with a blending radius of 2 mm. The E-plane T-junction geometrical parameters and simulated scattering parameters are reported in Table 3 and Figure 8, respectively. The return loss is better than 20 dB from 9.24 to 9.81 GHz, corresponding to a 5.98% fractional bandwidth. Equal power division is observed in the same frequency interval.

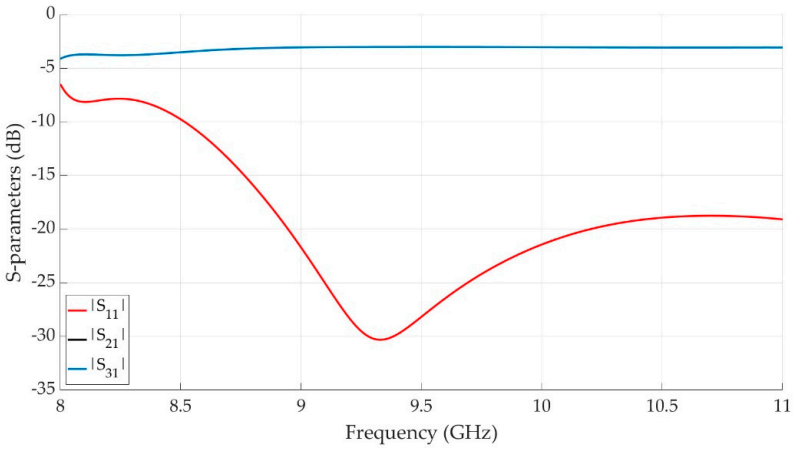

Figure 6. H-plane T-junction scattering parameters. S_{21} and S_{31} are identical.

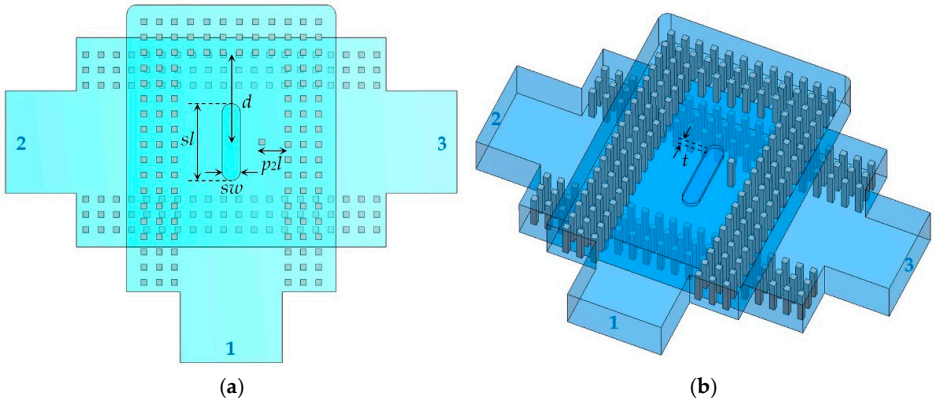

Figure 7. E-plane T-junction geometry. (**a**) Top view. (**b**) 3D view.

Table 3. E-plane T-junction geometrical parameters.

Parameter	Description	Value (mm)
d	Short distance	18.35
p_2l	Post 2 length	5.50
sl	Slot length	16.34
sw	Slot width	3.85
t	Slot thickness	1.00

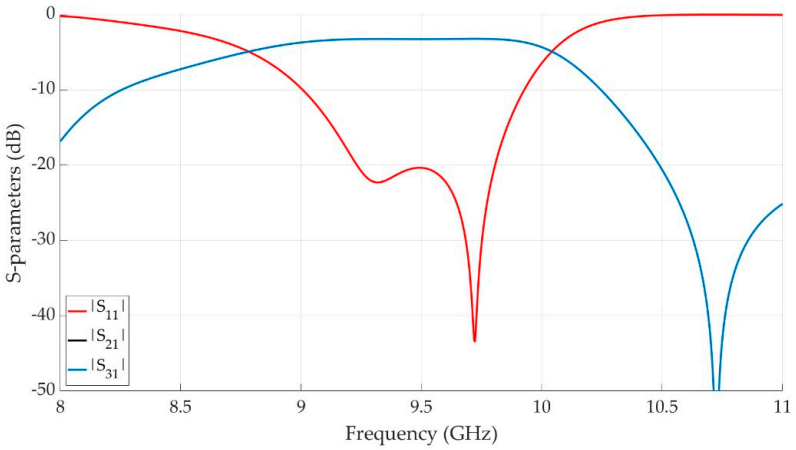

Figure 8. E-plane T-junction scattering parameters. S_{21} and S_{31} are identical.

4. Magic-T Design

The superposition of the two junctions of Section 3 generates a GGW magic-T. Depending on whether the sum and difference ports point in the same or opposite directions, two configurations can be derived, namely the T-shaped (TMT) one and the cross-shaped (XMT) one in Figure 9.

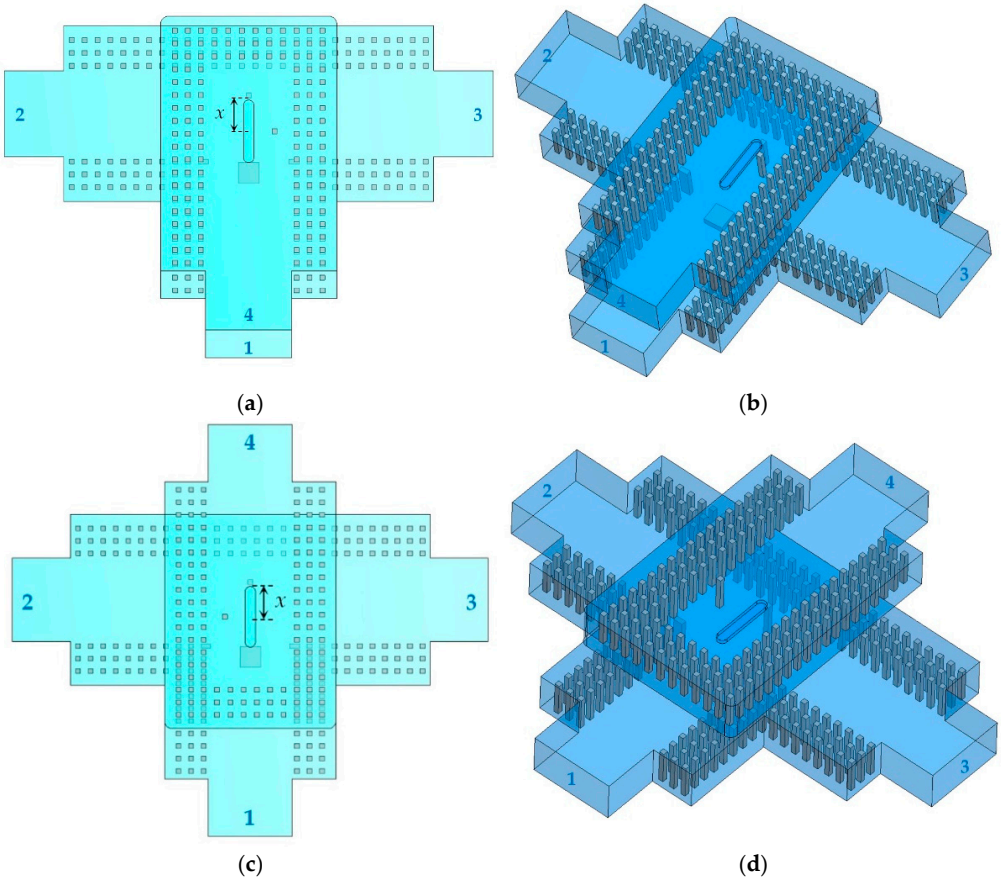

Figure 9. Magic-T geometry. (**a**) TMT top view. (**b**) TMT 3D view. (**c**) XMT top view. (**d**) XMT 3D view.

The geometrical parameters remain the same with respect to the H-plane and E-plane T-junctions, with the only exception of introducing parameter x, indicating the distance between the coupling slot center and the matching post in the lower layer. Port numbers 1, 4, 2 and 3 indicate the sum port, the difference port and the co-linear ports, respectively.

Since the T-junctions are not two completely independent structures, the geometrical parameter values need a full-wave local optimization for the design of the two magic-Ts. Both the TMT and XMT are simulated in the frequency-domain using the CST Microwave Studio "Trust Region Framework" built-in optimization algorithm. The geometrical parameters for the two configurations are listed in Table 4. Internal edges are rounded with a blending radius of 2 mm.

Simulated scattering parameters for both devices are reported in Figures 10 and 11. For the TMT, port matching is better than 20 dB for all ports in the frequency interval ranging from 9.25 to 9.75 GHz. In the same bandwidth, the isolation levels between the co-linear ports and the sum and difference ports are greater than 22 dB and 43 dB, respectively. For the XMT, port matching is better than 20 dB for all ports in the frequency interval ranging from 9.25 to 9.75 GHz. In the same bandwidth, the isolation levels between the co-linear ports and the sum and difference ports are greater than 22 dB and 43 dB, respectively.

Although the posts in the upper layers introduce an asymmetry in the overall geometries, transmission coefficients are not severely affected, showing a 3-dB power division with very low amplitude imbalances and correct phase differences in the above-mentioned bandwidth.

Table 4. Magic-T geometrical parameters.

Parameter	Description	TMT Value (mm)	XMT Value (mm)
bh	Block height	1.77	1.80
bl	Block length	5.24	5.31
bx	Block offset	3.45	3.38
d	Short distance	18.27	18.32
il	Iris length	2.53	2.43
p_1l	Post 1 length	7.48	7.44
p_2l	Post 2 length	5.52	5.51
sl	Slot length	15.79	15.74
sw	Slot width	2.62	2.63
t	Slot thickness	1.00	1.00
x	Slot offset	8.40	8.42

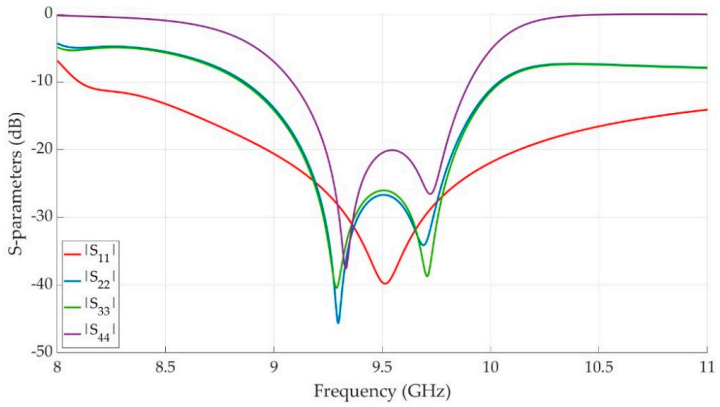

(**a**)

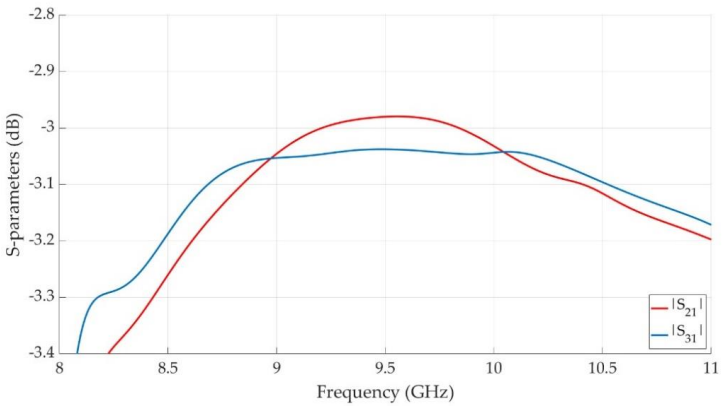

(**b**)

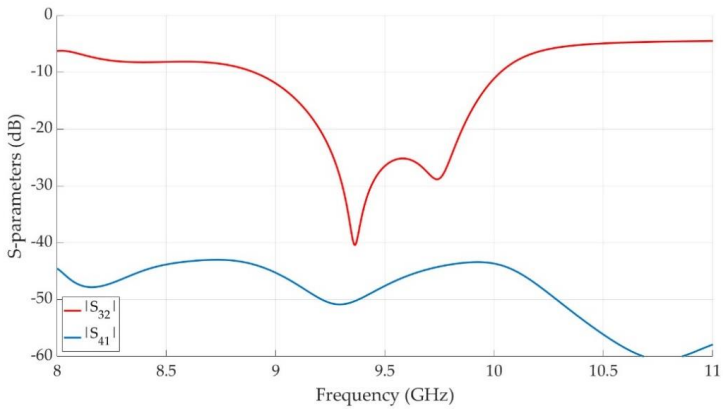

(**c**)

Figure 10. *Cont.*

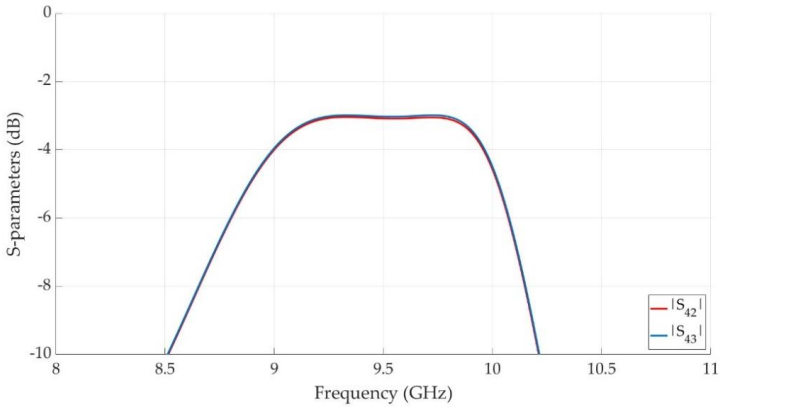

(**d**)

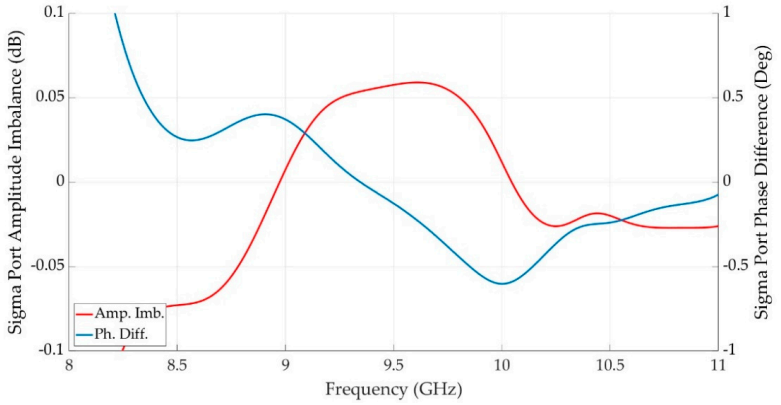

(**e**)

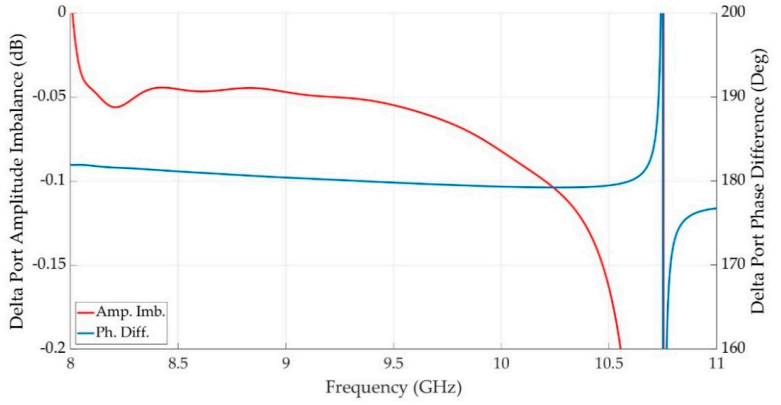

(**f**)

Figure 10. TMT simulated scattering parameters. (**a**) Port matching. (**b**) Port isolation. (**c**) Transmission coefficients (sum port excited). (**d**) Transmission coefficients (difference port excited). (**e**) Amplitude imbalance and phase difference (sum port excited). (**f**) Amplitude imbalance and phase difference (difference port excited).

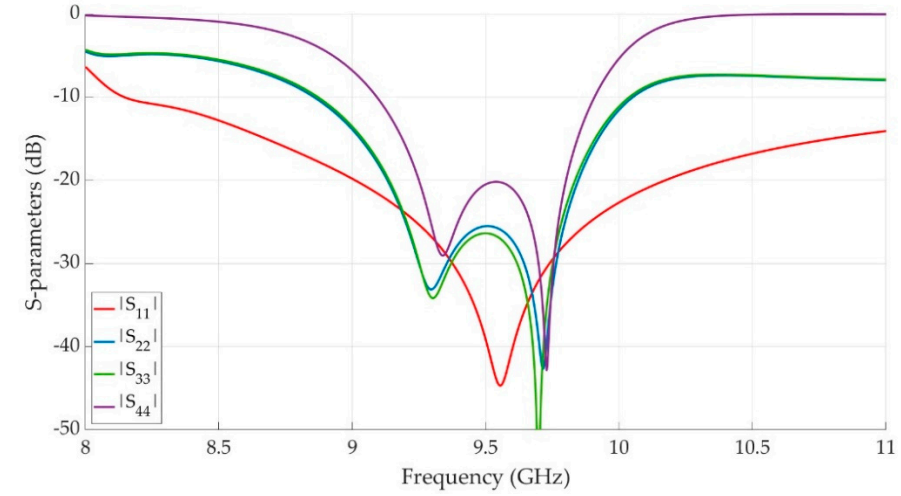

(**a**)

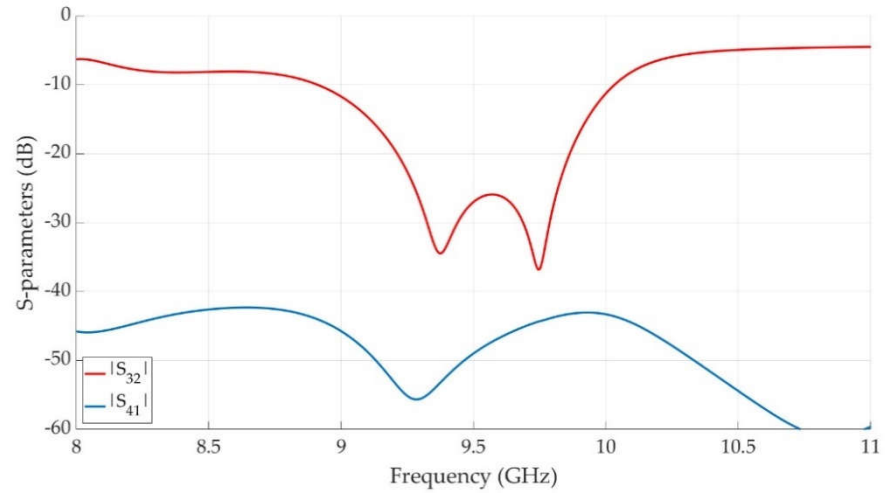

(**b**)

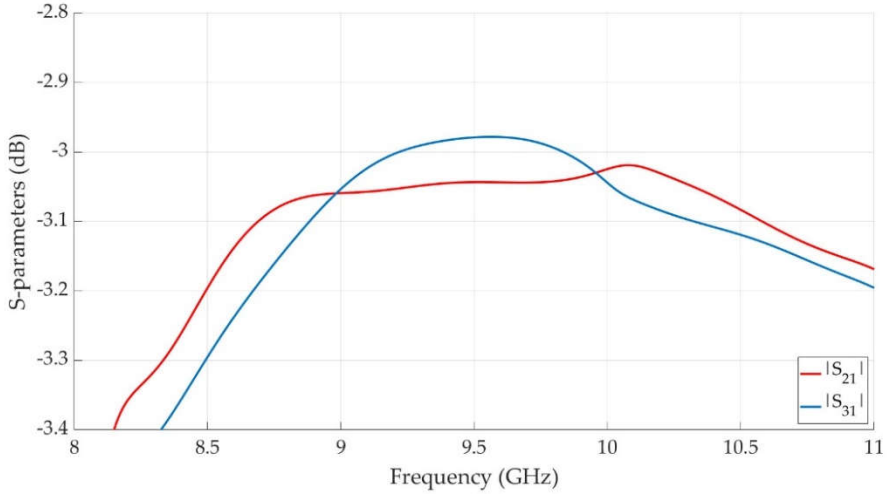

(**c**)

Figure 11. *Cont.*

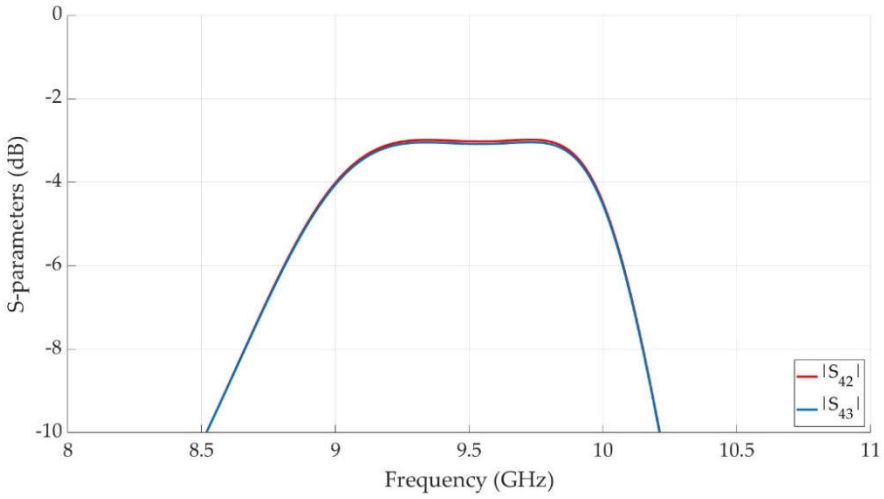

(**d**)

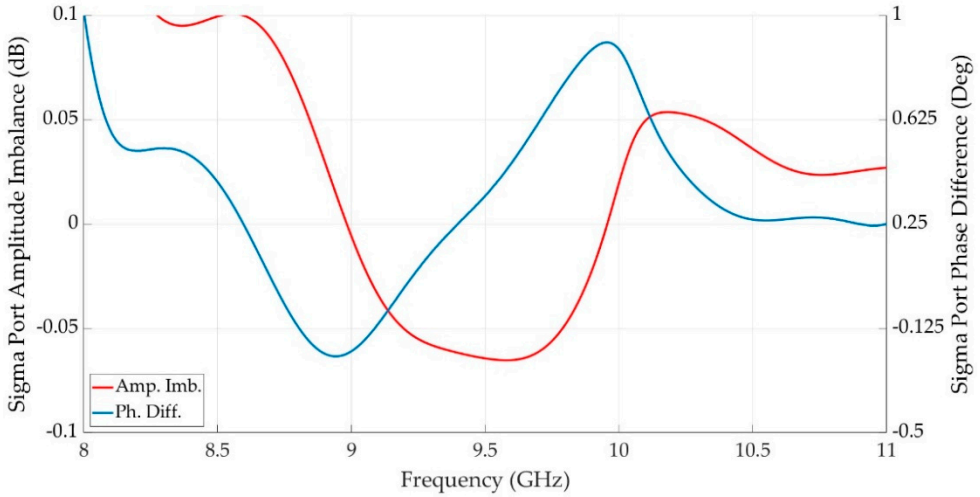

(**e**)

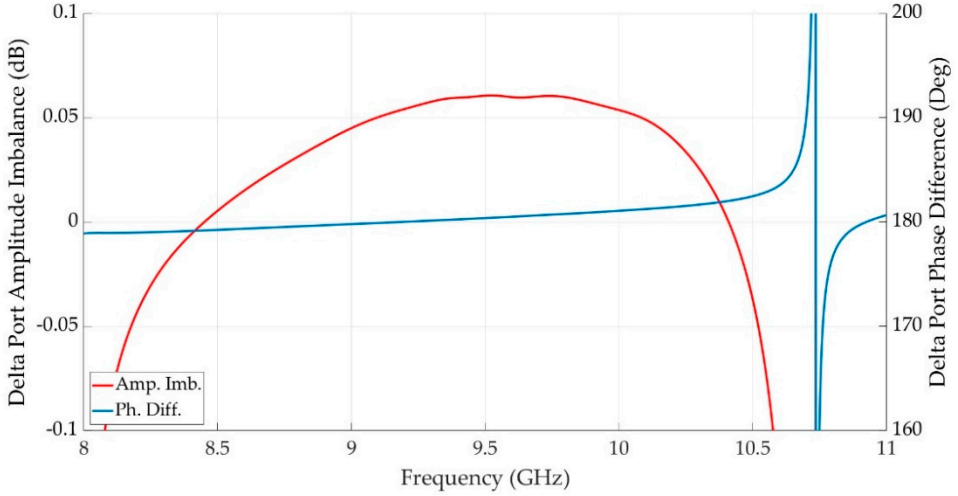

(**f**)

Figure 11. XMT simulated scattering parameters. (**a**) Port matching. (**b**) Port isolation. (**c**) Transmission coefficients (sum port excited). (**d**) Transmission coefficients (difference port excited). (**e**) Amplitude imbalance and phase difference (sum port excited). (**f**) Amplitude imbalance and phase difference (difference port excited).

5. Magic-T Manufacturing and Test

An XMT prototype is fabricated with aluminum using a low-cost CNC milling machine manufacturing process. The device is shown in Figure 12 and consists of three split blocks, in particular a bottom layer comprising the sum and co-linear ports, a central layer including the coupling slot and the difference port and an upper smooth cover plate. In order to feed the component, an in-line coaxial-to-groove gap waveguide transition is adopted for the four input ports, employing a three-step ridged section connected to the inner conductor of a coaxial line. To the best of the authors' knowledge, this is the first time that a transition of this kind is used to feed a GGW device. Further details on such transition can be found in Ref. [35], such as a tolerance analysis on the most critical geometrical parameters, showing the suitability of the adopted manufacturing process clearly. The three layers are assembled with a number of alignment screws and four SMA connectors.

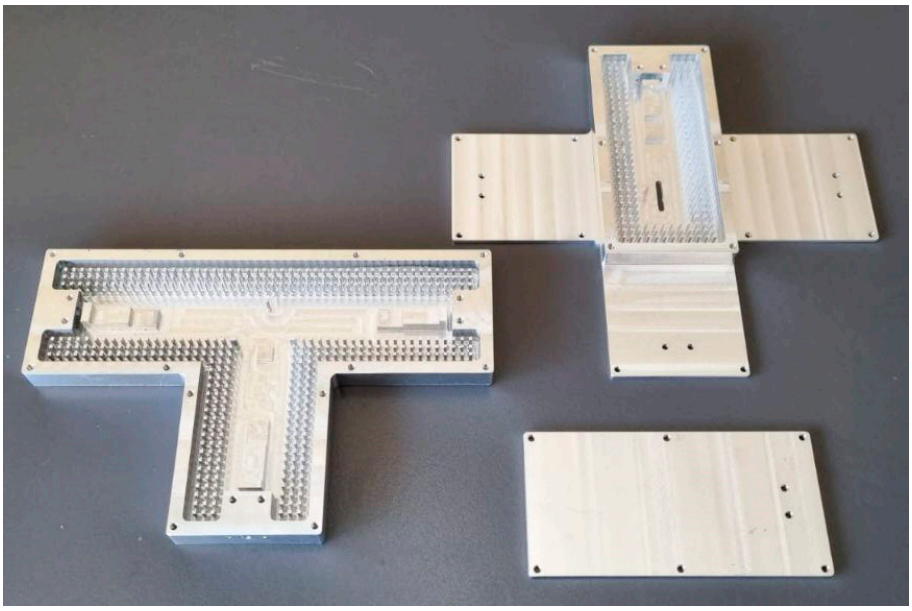

(**a**)

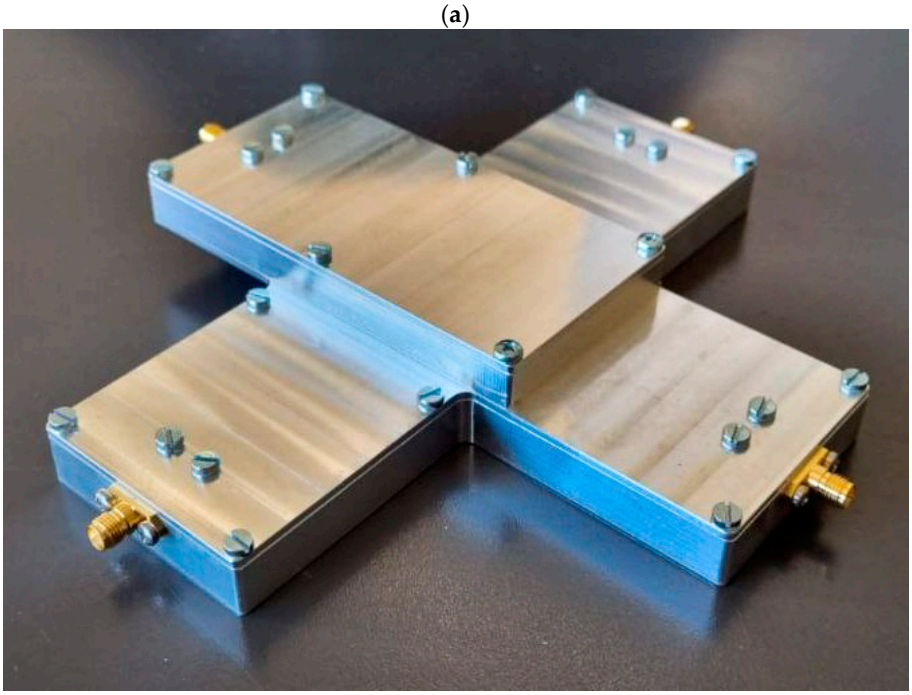

(**b**)

Figure 12. Manufactured X-shaped magic-T. (**a**) Separate layers. (**b**) Assembled prototype.

The XMT is tested with an Agilent N5230A vector network analyzer using the well-known full 2-port Short-Open-Load-Through (SOLT) calibration technique. Measured scattering parameters are compared with simulated results and reported in Figure 13.

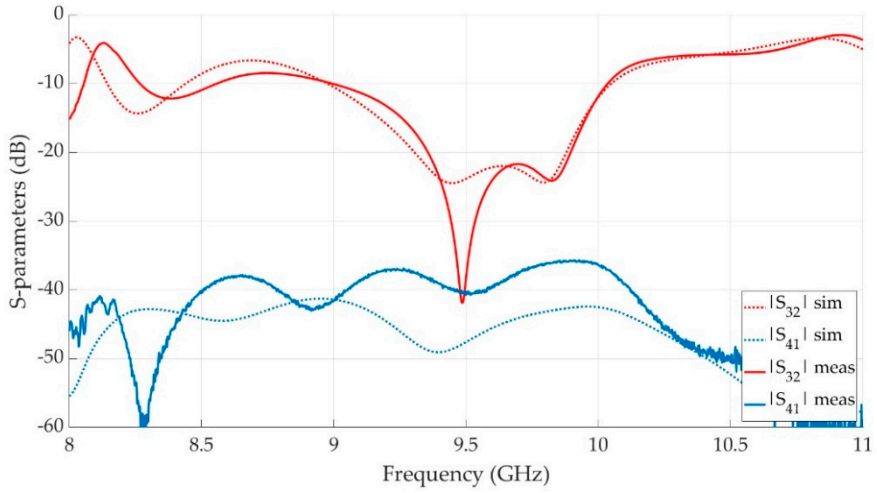

(**a**)

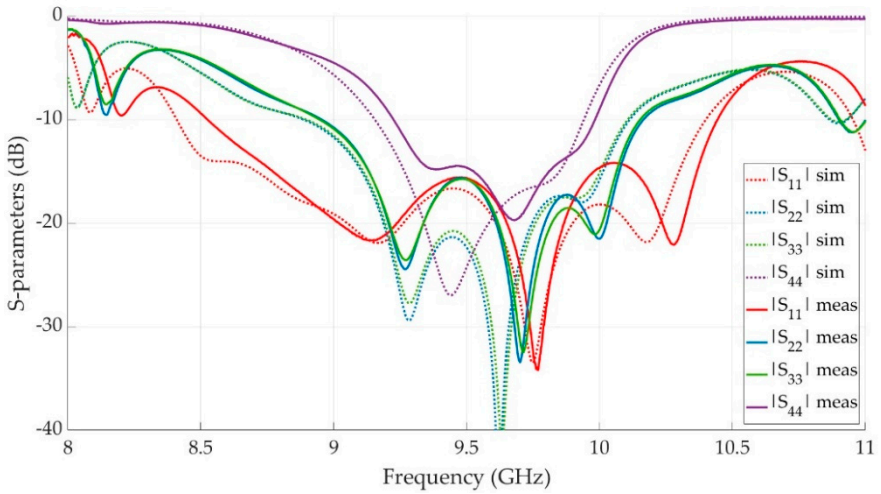

(**b**)

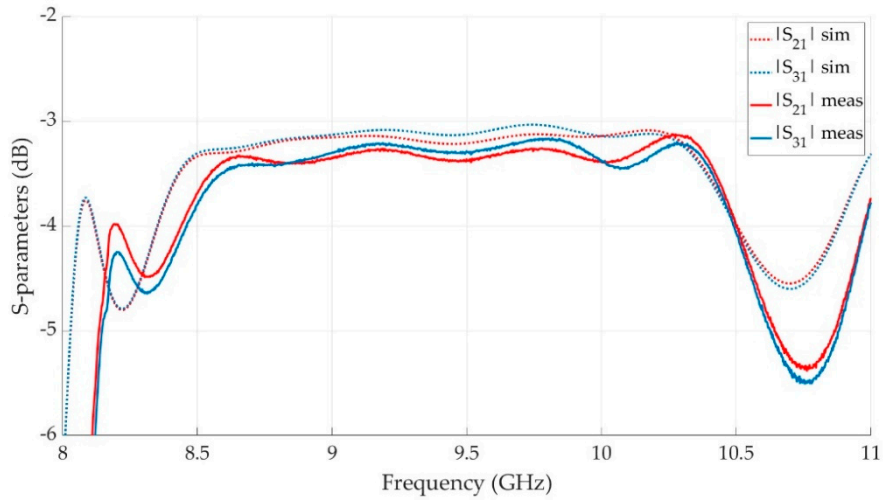

(**c**)

Figure 13. *Cont.*

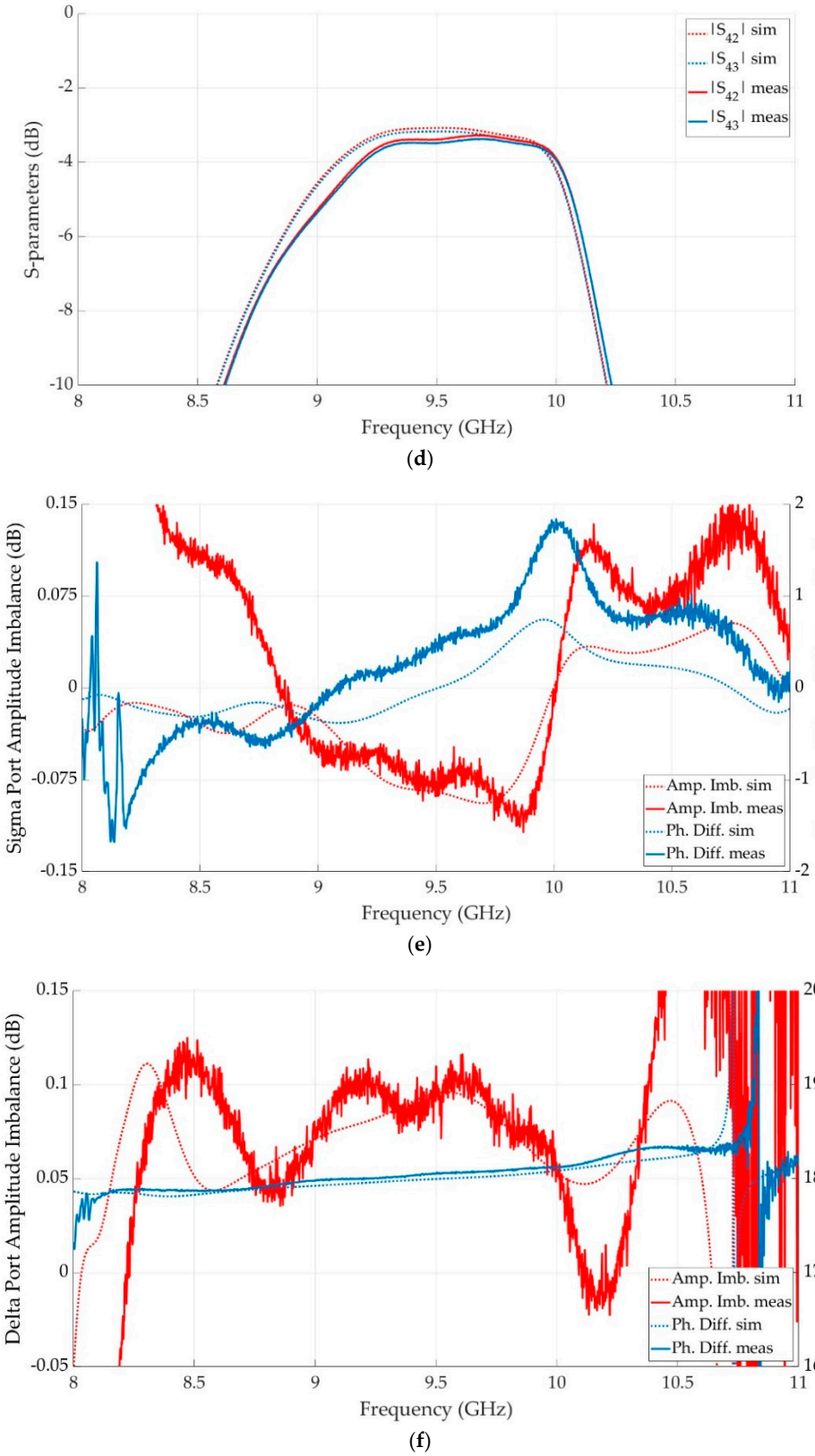

Figure 13. XMT measured scattering parameters. (**a**) Port matching. (**b**) Port isolation. (**c**) Transmission coefficients (sum port excited). (**d**) Transmission coefficients (difference port excited). (**e**) Amplitude imbalance and phase difference (sum port excited). (**f**) Amplitude imbalance and phase difference (difference port excited).

The adopted material in the simulation is aluminum with an equivalent conductivity of 2×10^7 S/m. This is a realistic value which deviates from the aluminum theoretical conductivity to compensate for surface roughness originating from a standard CNC manufacturing. Despite minor frequency shifts, the results are in very good agreement in the bandwidth 9.25–9.75 GHz, both in terms of scattering parameters and calculated amplitude imbalances and phase differences. The transmission coefficients present an average insertion loss of 0.3 dB in this frequency range, which is mainly due to the coaxial connectors. The small discrepancy between measured and simulated insertion loss is due to the SMA connectors, assumed as lossless in the simulation. The worsened isolation level for S_{41} is to be imputed to manufacturing tolerances in the order of ± 0.05 mm and to an imperfect alignment. Nevertheless, an isolation better than 37 dB in the specified bandwidth can be considered very good for a low-cost manufacturing process.

6. Conclusions

An H-plane and an E-plane T-junction in GGW technology was presented and combined in the design of a GGW magic-T operating at X band. This device was presented in two configurations, that is, with the sum and difference ports pointing in the same or opposite directions. A proof-of-concept prototype was realized with a low-cost CNC milling machine manufacturing process and tested to validate the design procedure. In spite of minor frequency shifts due to manufacturing tolerances and assembly, simulated and measured results have shown very good agreement. Thanks to the slot coupling feature, this magic-T can be adopted in all GGW circuits where a low-profile is required.

Author Contributions: Conceptualization, R.V.G. and R.R.; methodology, R.V.G. and R.R.; software, R.V.G.; validation, R.V.G. and R.R.; formal analysis, R.V.G. and R.R.; investigation, R.R.; resources, R.V.G.; data curation, R.R.; writing—original draft preparation, R.R.; writing—review and editing, R.V.G. and R.R.; visualization, R.R.; supervision, R.V.G.; project administration, R.V.G.; funding acquisition, R.V.G. All authors have read and agreed to the published version of the manuscript.

Funding: This research received no external funding.

Institutional Review Board Statement: Not applicable.

Informed Consent Statement: Not applicable.

Data Availability Statement: Not applicable.

Conflicts of Interest: The authors declare no conflict of interest.

References

1. Pozar, D.M. *Microwave Engineering*, 4th ed.; John Wiley and Sons: Hoboken, NJ, USA, 2011.
2. Chou, P.-J.; Lin, P.-C.; Lin, Y.-W.; Lu, J.-C.; Chang, C.-Y. Broadband planar magic-T with marchand type power divider and balun. In Proceedings of the 2014 Asia-Pacific Microwave Conference, Sendai, Japan, 4–7 November 2014; pp. 94–96.
3. U-Yen, K.; Wollack, E.J.; Papapolymerou, J.; Laskar, J. A Broadband Planar Magic-T Using Microstrip–Slotline Transitions. *IEEE Trans. Microw. Theory Tech.* **2008**, *56*, 172–177. [CrossRef]
4. Wang, Y.; Ma, K.; Mou, S. A Low-Loss Self-Packaged Magic-T With Compact Size Using SISL Technology. *IEEE Microw. Wirel. Compon. Lett.* **2018**, *28*, 13–15. [CrossRef]
5. Mansouree, M.; Yahaghi, A. Planar Magic-Tee Using Substrate Integrated Waveguide Based on Mode-Conversion Technique. *IEEE Microw. Wirel. Compon. Lett.* **2016**, *26*, 307–309. [CrossRef]
6. Zhu, F.; Hong, W.; Chen, J.-X.; Wu, K. Design and Implementation of a Broadband Substrate Integrated Waveguide Magic-T. *IEEE Microw. Wirel. Compon. Lett.* **2012**, *22*, 630–632. [CrossRef]
7. Feng, W.; Che, W.; Deng, K. Compact Planar Magic-T Using E-Plane Substrate Integrated Waveguide (SIW) Power Divider and Slotline Transition. *IEEE Microw. Wirel. Compon. Lett.* **2010**, *20*, 331–333. [CrossRef]
8. He, F.F.; Wu, K.; Hong, W.; Tang, H.J.; Zhu, H.B.; Chen, J.X. A Planar Magic-T Using Substrate Integrated Circuits Concept. *IEEE Microw. Wirel. Compon. Lett.* **2008**, *18*, 386–388. [CrossRef]
9. Peng, W.; Xiao, Q.; Chen, X. K-Band Planar Magic-T Using LTCC Technology. *IEEE Microw. Wirel. Compon. Lett.* **2017**, *27*, 715–717. [CrossRef]
10. Shen, T.-M.; Huang, T.-Y.; Chen, C.-F.; Wu, R.-B. A Laminated Waveguide Magic-T With Bandpass Filter Response in Multilayer LTCC. *IEEE Trans. Microw. Theory Tech.* **2011**, *59*, 584–592. [CrossRef]

11. Guo, C.; Gao, Y.; Wang, Y.; Huang, G.-L.; Cheng, Q.S.; Zhang, A.; Li, J.; Yu, Y.; Zhang, F.; Zhu, Y.; et al. A 3-D Printed E-Plane Waveguide Magic-T Using Air-Filled Coax-to-Waveguide Transitions. *IEEE Trans. Microw. Theory Tech.* **2019**, *67*, 4984–4994. [CrossRef]
12. Vincenti Gatti, R.; Rossi, R.; Dionigi, M.; Spigarelli, A. An X-band compact and low-profile waveguide magic-T. *Int. J. RF Microw. Comput. Eng.* **2019**, *29*, e21854. [CrossRef]
13. Kumar, V.S.; Kurup, D.G. A New Broadband Magic Tee Design for Ka-Band Satellite Communications. *IEEE Microw. Wirel. Compon. Lett.* **2019**, *29*, 92–94. [CrossRef]
14. He, Y.-J.; Mo, D.-Y.; Wu, Q.-S.; Chu, Q.-X. A Ka-Band Waveguide Magic-T With Coplanar Arms Using Ridge-Waveguide Transition. *IEEE Microw. Wirel. Compon. Lett.* **2017**, *27*, 965–967. [CrossRef]
15. Guo, L.; Li, J.; Huang, W.; Shao, H.; Ba, T.; Jiang, T.; Jiang, Y.; Deng, G. A Waveguide Magic-T With Coplanar Arms for High-Power Solid-State Power Combining. *IEEE Trans. Microw. Theory Tech.* **2017**, *65*, 2942–2952. [CrossRef]
16. Li, Y.; Zhang, Y.; Zhu, G.; Sun, Z.; Fan, Y. A w-band miniature power divider based on e-faced-folded magic-T junction. In Proceedings of the 2016 IEEE MTT-S International Microwave Workshop Series on Advanced Materials and Processes for RF and THz Applications (IMWS-AMP), Chengdu, China, 20–22 July 2016; pp. 1–3. [CrossRef]
17. Wang, Y.; Dou, W.; Bi, B. W band axially displaced monopulse dual-reflector antenna for inter-satellite communications. *IET Microw. Antennas Propag.* **2016**, *10*, 742–747. [CrossRef]
18. Gholami, M.; Amaya, R.E.; Yagoub, M.C. Low-loss compact power combiner for solid state power amplifiers with high reliability. *IET Microw. Antennas Propag.* **2016**, *10*, 310–317. [CrossRef]
19. Huang, G.-L.; Zhou, S.-G.; Chio, T.-H.; Yeo, T.-S. Two types of waveguide comparator for wideband monopulse antenna array application. In Proceedings of the IEEE 5th Asia-Pacific Conference on Synthetic Aperture Radar (APSAR), Singapore, 1–4 September 2015; pp. 264–266. [CrossRef]
20. Wang, L.; Shi, B. A method of design ka-band e-faced-folded compact waveguide magic-T junction. In Proceedings of the 3rd Asia-Pacific Conference on Antennas and Propagation, Harbin, China, 26–29 July 2014; pp. 1159–1161. [CrossRef]
21. Chu, Q.-X.; Wu, Q.-S.; Mo, D.-Y. A Ka-Band E-Plane Waveguide Magic-T With Coplanar Arms. *IEEE Trans. Microw. Theory Tech.* **2014**, *62*, 2673–2679. [CrossRef]
22. Leal-Sevillano, C.A.; Ruiz-Cruz, J.A.; Montejo-Garai, J.R.; Rebollar, J.M. Compact broadband couplers based on the waveguide magic-T junction. In Proceedings of the European Microwave Conference, Nuremberg, Germany, 6–10 October 2013; pp. 151–154. [CrossRef]
23. Zhu, Z.; Dong, S.; Wang, Y.; Dong, Y. A design of k band e-plane folded magic tee matched in two ways for spatial power combining. In Proceedings of the International Conference on Electronics, Communications and Control (ICECC), Ningbo, China, 9–11 September 2011; pp. 4078–4081. [CrossRef]
24. Hwang, K.C. Design and Optimization of a Broadband Waveguide Magic-T Using a Stepped Conducting Cone. *IEEE Microw. Wirel. Compon. Lett.* **2009**, *19*, 539–541. [CrossRef]
25. Chen, Z.N.; Liu, D.; Nakano, H.; Qing, X.; Zwick, T. *Handbook of Antenna Technologies*; Springer: Singapore, 2016.
26. Rajo-Iglesias, E.; Ferrando-Rocher, M.; Zaman, A.U. Gap Waveguide Technology for Millimeter-Wave Antenna Systems. *IEEE Commun. Mag.* **2018**, *56*, 14–20. [CrossRef]
27. Nasri, M.; Zarifi, D. A broadband gap waveguide-based magic-T junction for millimeter-wave applications. *Springer J. Infrared Milli. Terahz. Waves* **2021**, *42*, 793–801. [CrossRef]
28. Vosoogh, A.; Haddadi, A.; Zaman, A.U.; Yang, J.; Zirath, H.; Kishk, A.A. W-Band Low-Profile Monopulse Slot Array Antenna Based on Gap Waveguide Corporate-Feed Network. *IEEE Trans. Antennas Propag.* **2018**, *66*, 6997–7009. [CrossRef]
29. Cheng, X.; Zhang, Q.; Yao, Y.; Wang, C.; Yu, T.; Yu, J.; Chen, X. W-Band Binary Phase-controlled Multibeam Antenna Array Based on Gap Waveguide Magic-Tee. *IEEE Trans. Antennas Propag.* **2022**, *70*, 1. [CrossRef]
30. Farahbakhsh, A. Ka-Band Coplanar Magic-T Based on Gap Waveguide Technology. *IEEE Microw. Wirel. Compon. Lett.* **2020**, *30*, 853–856. [CrossRef]
31. Khandani, A.K.; Farahbakhsh, A. Ka-band planar magic-T based on e-plane groove gap waveguide for monopulse antenna system. In Proceedings of the 14th European Conference on Antennas and Propagation (EuCAP), Copenhagen, Denmark, 15–20 March 2020; pp. 1–3. [CrossRef]
32. Rajo-Iglesias, E.; Kildal, P.-S. Numerical studies of bandwidth of parallel-plate cut-off realised by a bed of nails, corrugations and mushroom-type electromagnetic bandgap for use in gap waveguides. *IET Microw. Antennas Propag.* **2011**, *5*, 282–289. [CrossRef]
33. Kildal, P.-S.; Zaman, A.; Rajo-Iglesias, E.; Alfonso, E.; Valero-Nogueira, A. Design and experimental verification of ridge gap waveguide in bed of nails for parallel-plate mode suppression. *IET Microw. Antennas Propag.* **2011**, *5*, 262–270. [CrossRef]
34. Raza, H.; Yang, J.; Kildal, P.; Alfonso, E. Resemblance between gap waveguides and hollow waveguides. *IET Microw. Antennas Propag.* **2013**, *7*, 1221–1227. [CrossRef]
35. Rossi, R.; Vincenti Gatti, R. X-Band In-Line Coaxial-to-Groove Gap Waveguide Transition. *Electronics* **2022**, *11*, 2361. [CrossRef]